A new discrete wavelength BUV algorithm for consistent volcanic SO₂ retrievals from multiple satellite missions

Bradford L. Fisher[1], Nickolay A. Krotkov[2], Pawan K. Bhartia[2], Can Li[2,3], Simon Carn[4], Eric Hughes[5] and Peter J. T. Leonard[6]

5 [1]SSAI, 10210 Greenbelt Rd, Suite 600, Lanham MD, 20706, USA

[2]Atmospheric Chemistry and Dynamics Laboratory, NASA Goddard Space Flight Center, Greenbelt MD, 20771, USA

[3] Earth System Science Interdisciplinary Center, University of Maryland, College Park, MD, 20742, USA

10 [4] Geological and Mining Engineering and Sciences, Michigan Technological University, Houghton MI 49931, USA

[5] Miner & Kasch, 8174 Lark Brown Rd, #101, Eldridge, MD 21075.

[6] ADNET Systems, Inc., 7515 Mission Drive, Suite A100, Lanham, MD 20706

15

Correspondence to: Bradford.Fisher (bradford.fisher@ssaihq.com)

Abstract. This paper describes a new discrete wavelength algorithm developed for retrieving volcanic sulfur dioxide (SO₂) vertical column density (VCD) from UV observing satellites. The Multi-Satellite SO₂ algorithm (MS_SO2) simultaneously retrieves column densities of sulfur dioxide, ozone,
20 Lambertian Effective Reflectivity (LER) and its spectral dependence. It is used operationally to process measurements from the heritage Total Ozone Mapping Spectrometer (TOMS) on board NASA's Nimbus-7 satellite (N7/TOMS: 1978-1993) and from the current Earth Polychromatic Imaging Camera (EPIC) on board Deep Space Climate Observatory (DSCOVR: 2015-) from the Earth-Sun Lagrange (L1) orbit. Results from MS_SO2 algorithm for several volcanic cases were validated using the more
25 sensitive principal component analysis (PCA) algorithm. The PCA is an operational algorithm used by NASA to retrieve SO₂ from hyperspectral UV spectrometers, such as Ozone Monitoring Instrument (OMI) on board NASA's Earth Observing System Aura satellite and Ozone Mapping and Profiling Suite (OMPS) on board NASA-NOAA Suomi National Polar Partnership (S-NPP) satellite. For this comparative study, the PCA algorithm was modified to use the discrete wavelengths of the
30 Nimbus7/TOMS instrument. Our results demonstrate good agreement between the two retrievals for the largest volcanic eruptions of the satellite era, such as 1991 Pinatubo eruption. To estimate SO₂ retrieval

1

Atmospheric
Measurement
Techniques
Discussions

uncertainties we use radiative transfer simulations explicitly accounting for volcanic sulfate and ash aerosols. Our results suggest that the discrete-wavelength MS_SO2 algorithm, although less sensitive than hyperspectral PCA algorithm, can be adapted to retrieve volcanic SO_2 VCDs from contemporary hyperspectral UV instruments, such as OMI and OMPS, to create consistent, multi-satellite, long-term

5   volcanic SO_2 climate data records.

1 Introduction

Volcanic eruptions are an important natural driver of global climate change, but unlike other natural climate forcing (e.g., changes in Earth's orbit, solar irradiance), the magnitude of volcanic forcing is highly variable, largely unpredictable, and the effects are typically more transient. Of most interest are
10   the episodic, large injections of volcanic sulfur dioxide (SO_2) into the Earth's stratosphere by major explosive volcanic eruptions, the most recent example being the eruption of Pinatubo (Philippines) in June 1991 (e.g., Bluth et al., 1992; Guo et al., 2004). Stratospheric loading of volcanic SO_2 by major eruptions leads to the formation of sulfuric acid (or sulfate) aerosols that scatter incoming solar shortwave radiation and absorb outgoing thermal radiation over timescales of months to years, cooling
15   the troposphere and warming the stratosphere (e.g., Robock, 2000). Primary volcanic emissions of aerosols such as volcanic ash can also have atmospheric and climate impacts, but these are typically more short-lived. Volcanic eruptions can also release reactive halogen species into the atmosphere, such as chloride and bromide (Mankin and Coffey, 1984; Bobrowski et al., 2003; Kern et al., 2008). Halogens can impact the total column ozone amount and profile shape if injected into the lower
20   stratosphere (Solomon et al., 1998, Klobas et al., 2017), but sulfate aerosols are also required to catalyze the heterogeneous chemical reactions that can efficiently deplete ozone. Hence, to understand the impacts of volcanic eruptions on climate, and in order to predict possible outcomes in the event of a major eruption, long-term satellite measurements of volcanic SO_2 emissions are essential.

The satellite record of volcanic SO_2 emissions by major volcanic eruptions extends back to
25   1978, and has been derived from instruments operating in both the ultraviolet (UV) and infrared (IR) spectral regions (Fig. 1; e.g., Carn et al., 2003, 2016, 2019; Prata et al., 2003). Measurements in the UV have a longer heritage, since the first satellite detection of volcanic SO_2 was achieved by the UV Total Ozone Mapping Spectrometer (TOMS) in 1982 following the eruption of El Chichon (Mexico; Krueger, 1983; Krueger et al., 2008), and interference from volcanic SO_2 must be accounted for in order to
30   produce accurate, long-term UV measurements of ozone. UV measurements have greater sensitivity to the total atmospheric SO_2 column than IR retrievals and hence the former have been the mainstay of volcanic SO_2 monitoring during the satellite era to date. The volcanic SO_2 climatology from 1978-present (Fig. 1, Carn 2019) reveals highly variable inter-annual volcanic SO_2 forcing dominated by two

major eruptions (El Chichon in 1982 and Pinatubo in 1991), with the post-2000 period dominated by smaller eruptions. Although none of these smaller eruptions have, individually, produced measurable climate effects, collectively they have garnered significant interest as they may play an important role in sustaining the persistent, background stratospheric aerosol layer, which is an important factor in global
5   climate forcing (e.g., Solomon et al., 2011; Vernier et al., 2011; Ridley et al., 2014).

One of the key challenges in assembling a long-term, consistent, satellite-based volcanic SO_2 emissions climatology (e.g., Fig. 1) is merging measurements from sensors with different spectral coverage and resolution. This complicates any analysis of 'trends' in volcanic SO_2 loading (e.g., in the post-2000 period of moderate volcanic eruptions; Fig. 1) or comparisons of eruptions of similar
10 magnitude in different satellite instrumental eras. A step change in SO_2 sensitivity occurred when the multi-spectral, six-channel TOMS instruments were superseded by hyperspectral UV sensors, such as the Global Ozone Monitoring Experiment (GOME, 1995-2003; Khokhar et al., 2005), the Scanning Imaging Absorption Spectrometer for Atmospheric Chartography (SCIAMACHY, 2002-2012; Lee et al., 2008), the Ozone Monitoring Instrument (OMI, 2004- ; Krotkov et al., 2006) and the Ozone
15 Mapping and Profiler Suite (OMPS, 2012- ; Carn et al., 2015). This is manifested in Figure 1 by an increased number of detected volcanic eruptions with low SO_2 loading (<10 kt) after 2004 (note that GOME and SCIAMACHY measurements are not shown in Fig. 1), whereas rates of global volcanic activity have not changed significantly. UV SO_2 retrieval algorithms have also evolved substantially since the 1980s in response to advances from multi-spectral to hyperspectral sensors, improvements in
20 ozone retrievals, and efforts to account for volcanic ash and aerosol interference (e.g., Krueger et al., 1995, 2000; Krotkov et al., 1997, 2006; Yang et al., 2007, 2010; Li et al., 2013, 2017; Theys et al., 2015). However, to date there has been no attempt to develop a single algorithm that could be used to generate a long-term, consistent SO_2 climatology across multiple UV satellite missions. In this paper we describe a new Multi-Satellite SO_2 algorithm (MS_SO2) that is applicable to both multi-spectral (e.g.,
25 TOMS) and hyperspectral (e.g., OMI) UV measurements. As a first step in the generation of a multi-satellite volcanic SO_2 record, we apply the MS_SO2 algorithm to the Nimbus-7 TOMS (N7/TOMS) measurements (1978-1993) and present a reanalysis of some of the most significant eruptions of the N7/TOMS mission.
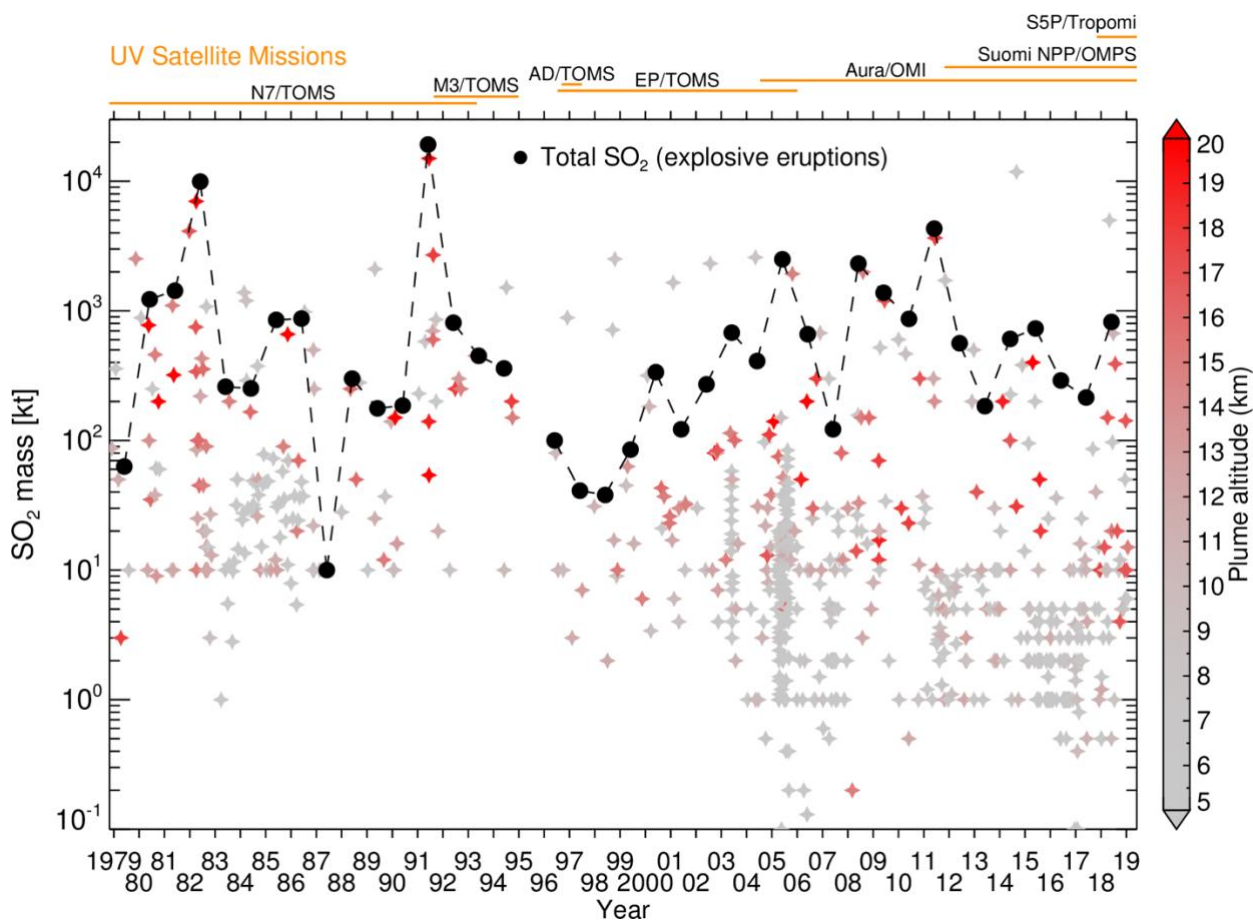
Atmospheric
Measurement
Techniques
Discussions

Figure 1. Multi-decadal record of SO₂ emissions by volcanic eruptions observed by NASA's fleet of satellites measuring TOA UV radiances. Eruptions (*star symbols*) are color-coded by estimated plume altitude, derived from a variety of sources, including Smithsonian Institution Global Volcanism

5 Program volcanic activity reports, volcanic ash advisories, and satellite data. The annual total explosive volcanic SO₂ production (omitting SO₂ discharge from effusive eruptions) is shown in black. *Orange lines* above the plot indicate the operational lifetimes of NASA UV satellite instruments: Nimbus-7 (N7), Meteor-3 (M3), ADEOS (AD), and Earth Probe (EP) TOMS, OMI (currently operational), and SNPP/OMPS (currently operational), along with the European Sentinel-5P/TROPOMI (currently

10 operational). Data shown in this plot are available from the NASA Goddard Earth Sciences (GES) Data and Information Services Center (DISC) as a level 4 MEaSUREs (Making Earth System Data Records for Use in Research Environments) data product (Carn 2019).

2 Heritage satellite ozone and SO₂ algorithms

Ozone and SO_2 are the two main absorbers in the near UV spectral region between 300 and 340 nm. The relative contributions of each gas to the satellite BUV measurements at the three absorbing TOMS channels used in the retrieval, depend on the spectral structure of the absorption cross sections, which are measured as functions of wavelength and temperature (Bogumil et al., 2003, Daumont et al. 1992). Figure 2 shows the O_3 and SO_2 cross sections and the SO_2/O_3 cross section ratio as a function of wavelength for a spectral UV region spanning the three absorbing channels (317, 331, 340 nm) of TOMS. At the instrument's spectral resolution (~1 nm FWHM) the SO_2 molecule is 2.5 times more absorbing than O_3 at 317 nm, while O_3 is 6 times more absorbing at 331 nm. These differences allow for simultaneous multispectral retrievals of O_3 and SO_2.
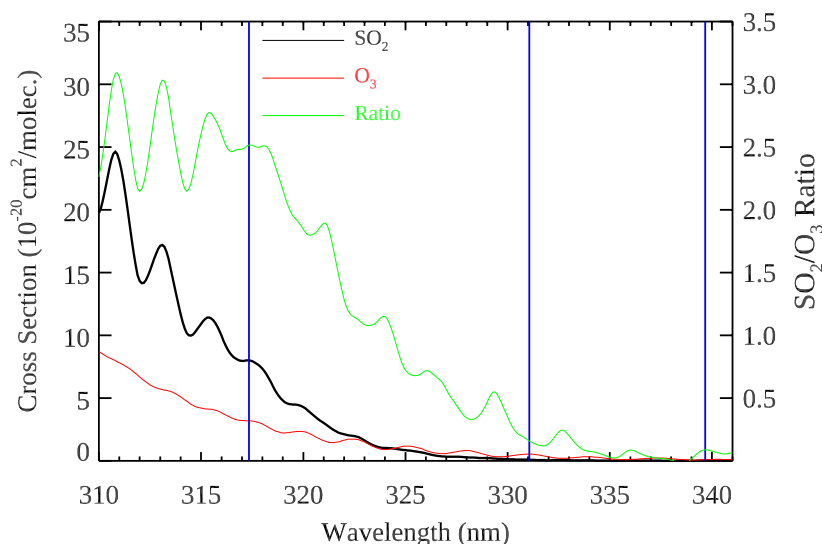

Figure 2. Spectral dependence of laboratory measured SO_2 (black) and O_3 (red) cross sections between 310-340 nm at TOMS spectral resolution (FWHM~1nm). The SO_2/O_3 ratio (green) is shown with the scale on the right axis. The nominal locations of the N7/TOMS absorbing bands (317, 331, 340 nm) are shown by vertical blue lines (blue).

2.1 Heritage BUV Ozone algorithms

Dave and Mateer (1967) first proposed a technique to estimate total ozone column from nadir backscatter UV measurements taken in the Huggins ozone absorption band (310-340 nm), assuming no SO_2 is present. Their algorithm was inspired by the pioneering Dobson Spectrophotometer which

Atmospheric
Measurement
Techniques
Discussions

measures attenuation of solar irradiance by UV wavelength pairs from which total ozone is derived, using the Beer-Lambert law. However, unlike the direct sun technique, radiative transfer calculations show that the top-of-the atmosphere BUV radiances (I) do not follow the Beer-Lambert law. In general, log(I) varies non-linearly with ozone column amount (Ω), and this relationship is sensitive to the shape

5   of the ozone profile (defined as the ozone density profile normalized to total ozone). To account for this effect Dave and Mateer (1967) proposed constructing a set of lookup tables (LUT) based on standard ozone profiles with different total ozone amounts using ozonesonde and Dobson Umkehr data. Since the shape of the profiles also vary with latitude, they proposed using three sets of profiles for low, mid and high latitudes. These profiles are then used to estimate I, which varies with wavelength (λ),

10   observational geometry, surface pressure and surface reflectivity (R). Following the Dobson convention, log(I) is converted to N-value which is defined in Eq. (1) as,

$$N = -100 log_{10}\left(\frac{I}{F}\right) \tag{1}$$

F is the extra-terrestrial solar irradiance. By linearly interpolating N between total ozone nodes, one forms the N-Ω curves that are a single valued function of Ω representative of a given latitude band and

15   observational geometry. This approach allows Ω to be estimated by matching the measured N-value to the interpolated N-values.

Over the years several modifications have been introduced to this basic concept. Mateer et al. (1971) proposed a Lambert-equivalent reflectivity (LER) concept to estimate the combined contribution of surface, clouds and aerosols to BUV radiance. In this concept, the scene at the bottom of the

20   atmosphere is assumed to be a Lambertian reflector whose reflectivity (R_s) is derived from the measurements at 380 nm where the ozone and SO_2 absorption is negligible. The effective pressure of this reflecting surface is assumed to vary with R_s, from a terrain pressure at $R_s < 0.2$ to a fixed cloud pressure 0.4 atm at $R_s > 0.6$, linearly interpolated at intermediate R_s. The algorithm assumed that R_s, thus derived, did not vary with wavelength. Although in the earlier versions of this algorithm

25   wavelength pairs (313/331, 318/340) were used to derive Ω, R_s was later derived at 331 nm to minimize errors due to the spectral dependence of R_s. This made pairing unnecessary (McPeters et al, TOMS User Guide).

By explicitly modelling the effect of aerosols using a radiative transfer code, Dave (1966) showed that R_s did not vary significantly with wavelength for non-absorbing aerosols, hence they

30   produced no ozone error. However, for aerosols that might have strong absorption in the UV, he predicted that R_s would decrease at shorter wavelengths, producing an overestimation of ozone. However, since aerosol properties in the UV were not known at that time, no correction for aerosol

Atmospheric
Measurement
Techniques
Open Access
Discussions
EGU

absorption was applied until the mid 90s when the effect predicted by Dave (1966) was detected in the Nimbus-7 TOMS data launched in October 1978.

Since the TOMS instrument had three reflectivity channels (331, 340, 380 nm), it was possible to compare the reflectivities derived from them. This comparison showed that R_s increased significantly

5   with wavelength for moderately thick clouds causing a significant underestimation of Ω (up to 3%). A modified LER (MLER) concept assuming two Lambertian surfaces, one at the surface and the other at the cloud top was applied to minimize this error (Ahmad et al., 2004).

The most recent version of the TOMS ozone algorithm reverts back to the LER model, but it assumes that clouds are at the surface, which reduces the R_s wavelength dependence (Ahmad et al.,

10   2004). An estimated ozone amount below the cloud is added to the derived Ω. However, since there are many other reasons for such a dependence including ocean color, non-Lambertian surfaces, such as ocean glint and fogbow, and most importantly the absorbing aerosol effect predicted by Dave (1966), R_s is assumed to vary linearly with λ; its slope is derived using 340 and 380 nm radiances. This simple omnibus approach works well for most cases, except when the UV absorbing aerosols (smoke, dust and

15   volcanic ash) are very thick. Such data are flagged in the TOMS ozone algorithm. The new MS_SO2 algorithm is an extension of this algorithm into two dimensions (section 3).

2.2 Heritage TOMS SO$_2$ algorithms

Krueger (1983) was the first to suggest that TOMS could be used to retrieve sulfur dioxide from explosive volcanic events. He correctly interpreted the large positive ozone anomaly observed following

20   the explosive eruption of El Chichon in 1982 as being due to the SO$_2$ released into the atmosphere during the event. To estimate the SO$_2$ inside the plume region, he separated the SO$_2$ and O$_3$ signals by computing a residual reflectance, estimated as the difference between the unperturbed background ozone outside the plume and the ozone anomaly inside the plume. This early technique for retrieving SO$_2$ from TOMS ozone estimates became known as the residual method. The residual method,

25   however, failed when the background could not be clearly separated from the ozone anomaly. Krueger subsequently developed the first BUV algorithm that separated the O$_3$ and SO$_2$ radiance contributions, based on an earlier methodology developed by Kerr (1980) to retrieve the SO$_2$ column from the ground with a Brewer spectrophotometer. This method assumed that the TOA backscattered radiation was attenuated by the two absorbing species (O$_3$, SO$_2$), leading to the Eq. (2) describing BUV radiance, I,

30   for a given wavelength, λ, corresponding to the TOMS field of view (FoV):

$$I(\lambda) = aF(\lambda)\exp\left[-b\lambda + Sg(\tau_{O_3} + \tau_{SO_2})\right], \qquad (2)$$

In Eq. (2), F is the incoming solar flux, S_g is the geometrical optical path (air-mass factor, AMF), and τ_{O3} and τ_{SO2} are the absorption optical thicknesses for O_3 and SO_2, while the coefficients a and b depend on the satellite viewing geometry, cloud/surface reflectance and volcanic ash and sulfate aerosols (Krueger et al., 1995, Krotkov et al., 1997). Equation 2 can be expressed in matrix form, which is then

5   inverted to obtain estimates for the SO_2 and O_3 vertical column densities and the dimensionless parameters a and b. This algorithm is generally referred to as the Krueger-Kerr algorithm (Krueger et al., 1995). Krotkov et al. (1997) developed radiative transfer path correction, which explicitly accounted for the R_s, ozone and SO_2 vertical profiles, replacing the geometrical AMF in Eq. (2). The modified algorithm with empirical background correction has been used off-line on a case-by-case basis for the

10   past two decades to retrieve SO_2 mass tonnage from medium to large explosive eruptions using TOMS BUV measurements (Krueger *et al.,* 2000; Carn *et al*., 2003).

3 New MS_SO2 algorithm

      The new discrete wavelength SO_2 algorithm (MS_SO2) builds on the heritage of the TOMS total ozone algorithm (section 2.1) but adds sulfur dioxide (SO_2) as a second absorber. The BUV

15   radiance is simulated with the TOMRAD forward vector radiative transfer (RT) model (Dave 1964) from a known viewing geometry by assuming a vertically inhomogeneous, pseudo-spherical Rayleigh scattering atmosphere with standard O_3 and a priori SO_2 vertical profiles. The underlying reflecting surfaces (land/ocean, clouds and aerosols) are approximated with the simple LER reflecting surface at terrain height pressure (section 2.1). TOMRAD accounts for all orders of polarized Rayleigh scattering

20   and for the gaseous absorption (i.e., O_3 and SO_2), using a priori vertical profiles of the gas concentrations and laboratory measured temperature dependent gaseous cross sections (Dave and Mateer, 1967, Bogumil et al., 2003, Daumont et al. 1992). Improvements to the TOMRAD model include corrections for molecular anisotropy (Ahmad and Bhartia, 1995), rotational Raman scattering (Joiner, 1995) and pseudo-spherical corrections to account for changes to the solar and viewing zenith

25   angles due to the sphericity of the earth.

      Performing on-line radiative transfer calculations for every satellite field-of-view (FoV) greatly increases the time required to process full orbits of data. To improve the computational efficiency of the operational algorithm, N7TOMS-specific look-up-tables (N7TOMS-LUT) were produced off-line using the inputs listed in Table 1 and convolved with the triangular band pass at each of the six Nimbus-7

30   TOMS wavelengths (FWHM~1 nm). For a given set of inputs, the five BUV radiance parameters, I_0, I_1, I_2, T and S_b are linearly interpolated from the N7TOMS-LUT and the total BUV radiance, I_c, , is calculated using Eq. (3):

$$I_c(\lambda, \theta_0, \theta_S, \phi, P, \Omega, \Sigma, R_S) = I_0 + I_1 \cos(\phi) + I_2 \cos(2\phi) + \frac{R_s T}{(1 - R_s s_b)}, \tag{3}$$

where, I_c is a function of wavelength, solar and satellite zenith viewing angles, relative azimuthal angle, surface pressure, a priori ozone and sulfur dioxide vertical profiles, and the underlying surface reflectivity, respectively. The I_c is converted to N-value, N_c, as defined in Eq. (1), and compared with the measured N-value, N_m during operational retrievals.

Table 1: Input parameters used in construction of the Nimbus-7 TOMS LUTs

TOMRAD-based LUT nodes		
LUT Node	Number of Nodes	Values
Surface Pressure	2	1013.25 and 500 hPa
Wavelength	6	312.5, 317, 331, 340, 360 and 380
Total Column Ozone	21	3 low, 8 middle and 11 high latitude bands (Dobson Units, DU)
Total Column SO$_2$	12	0, 5, 10, 50, 100, 150, 200, 250, 350, 450, 550, 650 (DU)
solar zenith angle SZA	10	0, 30, 45, 60, 70, 77, 81, 84, 86, 88
satellite zenith angle VZA	6	0, 15, 30, 45, 60, 70

The TOMRAD was configured to account for two absorbing trace gases: O_3 and SO_2. The LUTs include twenty-one total ozone nodes and twelve total SO_2 nodes for each of the three assumed SO_2 vertical profile shapes. For ozone, the total column amounts correspond to the standard profile shapes, which vary between three latitude bands (see Table 1). For sulfur dioxide, we assumed a Gaussian vertical profile shape, which is determined by two parameters: a center of mass altitude (CMA) and a geometrical standard deviation. The CMA represents the altitude of the peak SO_2 concentration. LUTs for SO_2 are generated for three different CMAs: 8 km (middle troposphere, TRM), 13 km (Upper Tropospheric/Lower Stratospheric, TRU), and 18 km (lower stratospheric, STL). A constant standard deviation of σ=2 km is assumed for each SO_2 profile.

The MS_SO2 algorithm retrieves a four-parameter state vector, **x,** defined below in Eq. (4) as,

$$x = \begin{pmatrix} \Sigma \\ \Omega \\ dRs/d\lambda \\ R_S \end{pmatrix}, \qquad (4)$$

where Σ is the retrieved total column sulfur dioxide, Ω is the total column ozone, $dR/d\lambda$ characterizes the R_s spectral dependence, and R_S is the LER at 380nm. The retrieval of sulfur dioxide is carried out in one or two steps described in the next sections, referred to as step 1 and step 2.

3.1 Step 1 retrieval

The state vector, x, is determined iteratively by inverting the Jacobian matrix $\mathbf{K}$ (Eq. 5) at each iteration step:

$$N = \mathbf{K}x, \qquad (5)$$

where N represents the measured vector of N-values for the four TOMS channels at 317, 331, 340 and 380 nm, and $\mathbf{K}$ represents a 4 x 4 Jacobian matrix derived from the LUTs. The matrix elements are defined as:

$$K_{i,j} = \frac{\partial N_{c\,i}}{\partial x_j}, \quad i,j = 1,4 \qquad (6)$$

where $N_{c,i}$ is the forward model calculated N-value at wavelength i.

Our step 1 inversion starts with an initial state vector $\mathbf{x_0}$, consisting of first guesses for Σ_0, Ω_0, and $dR_s/d\lambda$ shown in Table 2. Rs is computed analytically using the measured BUV radiance at 380 nm, before beginning the iteration (see Supplement, Eq. S2). Note that since the O_3 and SO_2 cross-sections are negligible at 380 nm, the Rs and $\partial N_{380}/\partial R_s$ do not change with the iterations (*i.e.,* dRs $= 0$).

Equation (5) is solved iteratively by zeroing the residuals, $dN=N_{meas}-N_c$, and re-computing the Jacobians at each iteration step for the four used spectral channels. The state vector is then adjusted after each iteration, $\mathbf{x} = \mathbf{x_0} + \mathbf{dx}_k$, until it converges on a solution (*i.e.,* $\mathbf{dx}_k \sim 0$), as described in Eq. (7) below:

$$dN_k = N_m - N_{c,k-1} = \mathbf{K}_{k-1}dx_k \qquad (7a)$$

$$dx_k = x_k - x_{k-1} = \mathbf{K}_{k-1}^{-1}dN_k \qquad (7b)$$

Since O_3 and SO_2 exhibit small absorption at 340 nm, a non-zero R spectral slope (i.e., dR/d$\lambda \neq 0$) accounts for the radiative effects of aerosols. As indicated in Table 2, the algorithm initially assumes no R-lambda dependence (i.e., dR/d$\lambda = 0$), however, absorbing and non-absorbing aerosols can cause dR/d$\lambda \neq 0$.

Atmospheric
Measurement
Techniques
Discussions

Table 2: State Vector

Retrieved Parameter	Wavelength (nm)	Symbol	First Guess[*]
Total Column SO_2	317	Σ	$\Sigma_0 = 0$
Total Column O_3	331	Ω	Ω_0
Spectral Reflectivity Dependence	340	dR/d_λ	$dR_0/d_\lambda = 0$
Reflectivity	380	R_S	N/A

[*]Ω_0 is a climatological value corresponding to one of three latitude bands

5 The algorithm uses the retrieved spectral slope, defined in Eq (8), to update the calculated LERs after each iteration:

$$R_j = R_S + \frac{\partial R}{\partial \lambda}(\lambda_j - \lambda_R), \quad j = 1, 4 \qquad (8)$$

where $\lambda_j = 312, 317, 331, 340$ nm and $\lambda_R = 380$ nm. When SO_2 or aerosol loading is high, non-linear
10 effects can cause the SO_2 Jacobian in Eq. (6) to become very small causing R(j) to deviate significantly from Eq. (8), especially at the shortest TOMS wavelength, 312nm. The non-linear spectral dependence of R(j) produces systematic errors in the retrieved state vector. For this reason, we do not use the 312 nm channel in the retrievals, but the final residual dN_{312} can be used as a diagnostic of the spectral non-linearity of the scene. A step 2 empirical procedure, described in the next section, was developed to
15 correct for the retrieval bias resulting from these errors.

3.2 Step 2 retrieval

The MS_SO2 forward model accounts for O_3 and SO_2 absorption and linear spectral changes in R_S due to the presences of aerosols. The algorithm, however, does not explicitly characterize the absorption and scattering effects of volcanic ash (absorbing) and sulfate (non-absorbing) aerosols. The
20 retrieval errors in Σ and Ω caused by volcanic ash during the first days after an explosive eruption can be significant in the case of major volcanic eruptions like Pinatubo and El Chichon (Krueger et al., 1995; Krotkov et al., 1997). A step 2 procedure was developed primarily to handle explosive eruptions (VEI > 3), in which large Ω anomalies are identified to occur in conjunction with high ash concentrations. In step 2, a corrected total ozone Ω_{cor} inside the SO_2 cloud is interpolated using the

retrieved Ω outside the plume along the orbit for each cross-track position. Even if ozone destroying halogens are present, such effects can still be considered negligible over the relatively short time periods that SO_2 concentrations are high enough to affect TOMS observations.

In deciding whether to apply Step 2, the algorithm considers the retrieved Σ, Ω and Aerosol
5   Index (AI) in Step 1. The AI is estimated from Eq. (9) from the Step 1 parameter dR/dλ and the calculated Jacobian dN/dR at 340 nm:

$$AI = \frac{\partial N_{340}}{\partial R}\frac{\partial R}{\partial \lambda}(\lambda_{340} - \lambda_{380}) = -40 \cdot \frac{\partial N_{340}}{\partial R}\frac{\partial R}{\partial \lambda}. \qquad (9)$$

Positive AI (dR/dλ>0) identifies spatial regions affected by absorbing aerosols (dust, smoke, ash). The step 2 selection criteria first select FoVs where either $SO_2 > 15$ DU (inside the plume) or AI > 6. The
10 additional AI criterion allows for the selection of FoVs around the edges of the cloud, where the SO_2 can be less than 15 DU due to high aerosol concentrations. In this case, it is assumed that the step 1 SO_2 may have been underestimated due to the ozone error caused by high aerosol concentrations (in these cases, the SO_2 retrieved in step 2 may still not exceed 15 DU, and therefore would be excluded from the plume in subsequent mass calculations). We describe the methodology for interpolating Ω_{cor} in
15 equations S3-S5 of the supplement. A second retrieval of SO_2 and dR/dλ is then performed by inversion using the measured 317 and 340 nm radiances while treating the ozone Ω_{cor} as a constant. This constraint on the ozone bounds the SO_2 Jacobians computed from the forward model LUTs. The operational MS_SO2 file includes a step 2 algorithm flag (not applied = 0, applied = 1).

To illustrate the effects of the step 2 procedure, we consider the 1982 explosive eruption of El
20 Chichon, which emitted ~7 Tg SO_2, the second largest observed in the satellite era (Fig.1). Figure 3 shows the retrieved AI map during TOMS overpass of the volcano on April 4, 1982, while it was still erupting. High AI values exceeding a value of 10 correspond to high biased step 1 ozone values (Fig. 4a) and underestimated Σ values (Fig 4c). Figure 4b shows the step 2 corrected Ω_{cor}, which is consistent with the Ω field outside of the volcanic cloud. Figure 4d shows the step 2 Σ, which is much higher than
25 retrieved in step 1. As can be seen in this particular example, the step 2 correction can significantly increase the SO_2 mass. In this case, the SO_2 mass increased from 2475 kilotons (step 1 to 3637 kilotons (step 2). Peak Σ values increased from 396 DU to 549 DU in the aerosol affected region. The biases, dΩ and dΣ, for this case are shown in Fig. S1 of the Supplement. Step 2 was developed primarily to handle extreme eruptions (VEI > 3), such as El Chichon and Pinatubo, where large Ω anomalies sometimes
30 occur in conjunction with high ash concentrations. In practice step 2 corrections tend to be small (or none at all) for most moderate eruptions detected during the observation period covered by Nimbus 7 TOMS.

 The step 2 Ω values inside the volcanic cloud shown in Fig. 4b appear to be fairly consistent with the surrounding ozone field, but there still exist a few remaining high Ω values in the boundary of the plume, which were not selected for step 2 (Fig. 4b). These pixels were not corrected because the threshold criteria were not met, so that Σ may be underestimated. However, their contribution to the total SO_2 cloud mass is insignificant.

5

Step 2 follows a methodology similar to the original residual method developed by Krueger (1983), which separated the O_3 and SO_2 contributions by subtracting the measured BUV reflectance in the unperturbed region from the BUV radiance anomaly associated with the SO_2 cloud. The MS_SO2 algorithm corrects the ozone inside the plume by removing the ozone anomaly. Our Step 2 procedure is typically only applied when the ash loading (i.e., high AI) causes the reflectivity dependence to become non-linear, as the forward model does not explicitly account for volcanic aerosol absorption. This scenario typically lasts for about 1-3 days following a major explosive eruption, during which total retrieved SO_2 mass is likely to be underestimated, and in some cases, could even increase with time due to ash and ice fallout and plume dispersion. For such extreme cases we recommend estimating SO_2 to sulfate conversion e-folding life-time using weeks' worth of measurements of the total SO_2 cloud daily mass and extrapolating it back in time to estimate total SO_2 mass emitted on eruption day. This "day one" time extrapolated SO_2 mass is typically larger than retrieved on days immediately following the eruption (Krotkov et al., 2010).
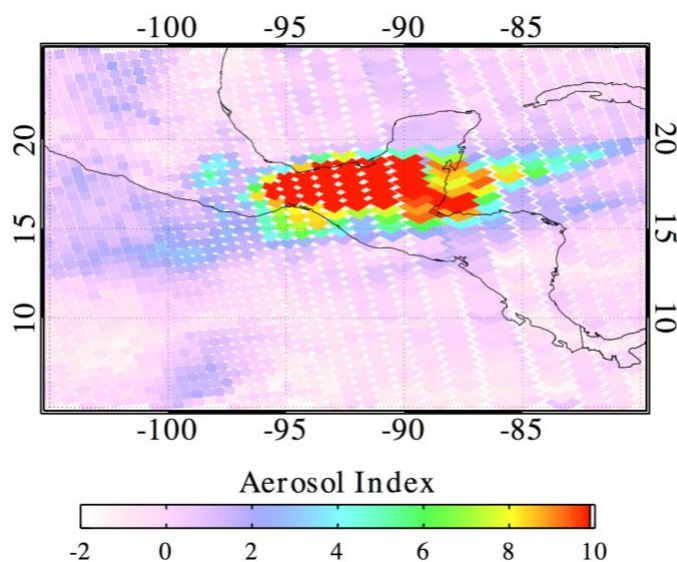
10

15

20

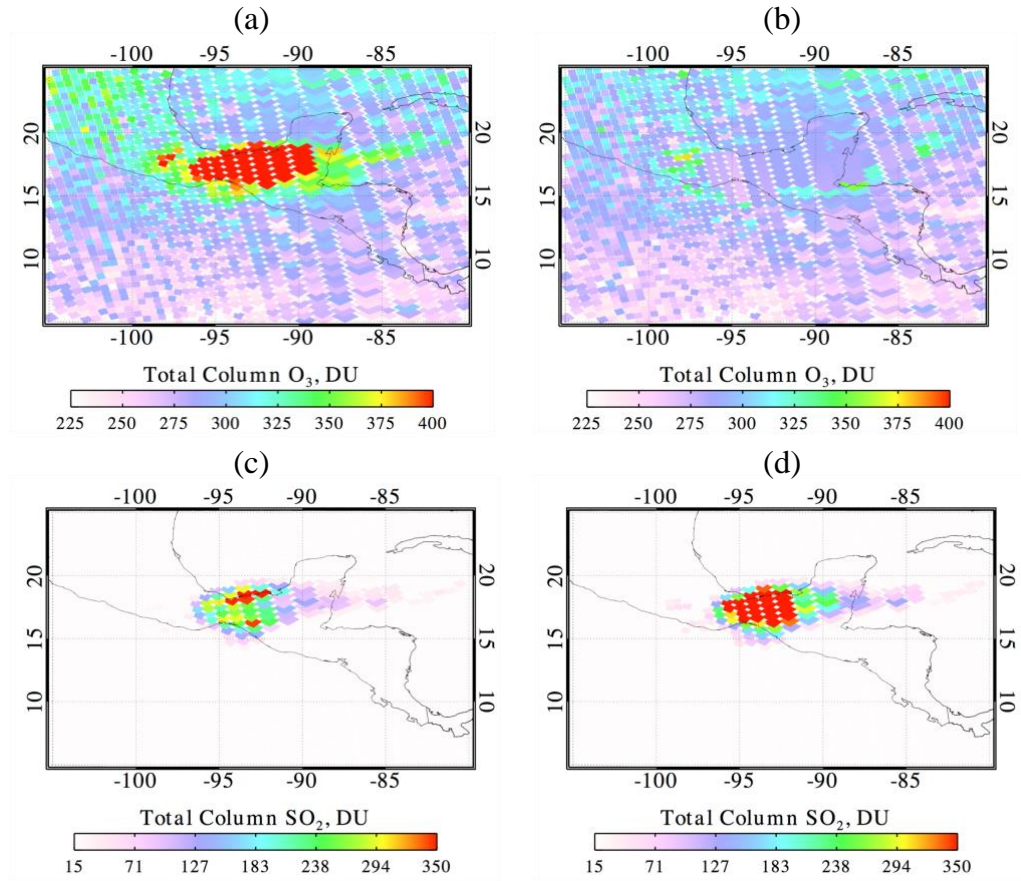**Figure 3.** Aerosol Index for the El Chichon eruption on April 4, 1982, computed from retrieved dR_λ.

13

Figure 4. MS_SO2 imagery showing a) Step 1 total column O_3, b) Step 2 total column O_3 c) Step 1 total column SO_2 and d) Step 2 total column SO_2 for the case of El Chichon eruption on April 4, 1982.

5

3.3 Soft Calibration: N-value bias correction

We assume that the background sulfur dioxide is below TOMS detection limit in regions of the atmosphere far away from any SO_2 sources (e.g., volcanic, anthropogenic). Random errors associated with the retrieval process, however, are normally distributed around zero. We expect that the true
10   volcanic SO_2, Σ_{true}, and the mean of the background SO_2 distribution, $\langle\Sigma\rangle_{clean}$, are zero:

$$\Sigma_{true} = \langle\Sigma\rangle_{clean} = 0 \qquad (10)$$

An examination of the measured Σ distribution in clean regions of the Central Pacific Ocean found a positive bias of about 3 DU (i.e., $\langle\Sigma\rangle_{clean}\sim$ 3 DU, Fig. 5). We correct for the bias by applying a

14

small fixed N-value adjustment at 340 nm as a function of the swath position (Figure 6). Figure 5b shows the effect of this adjustment on the step1 background Σ distribution (Fig. 5a). Figure 5c displays daily global SO_2 background map, and figure 5d shows the SO_2 difference map (after – before the correction). The details of this procedure are described in S3.3 of the supplement.
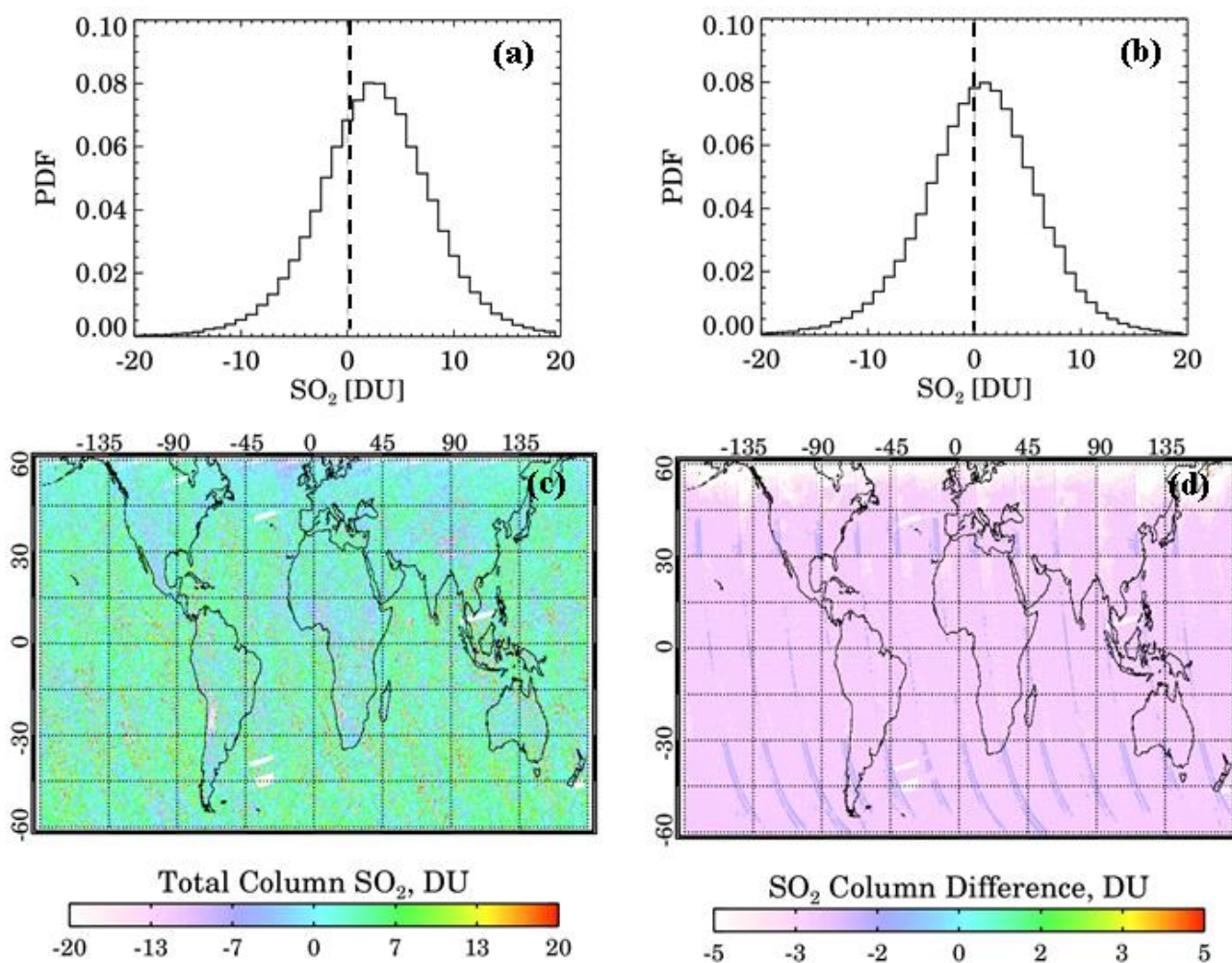
5

Figure 5. Probability density of function of SO_2 background a) before applying 340 N-value correction and b) after applying correction, c) global daily SO_2 map before applying 340 N-value correction, d) the difference (after correction – before correction) map.
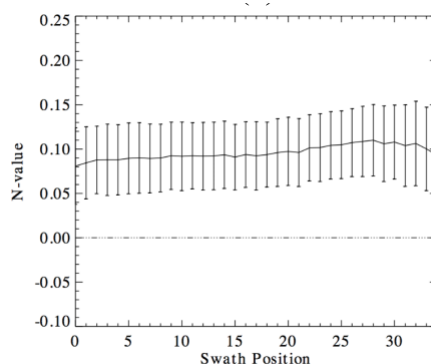
10

Figure 6. Mean 340 nm N-value adjustment with error bars computed from a sample of 90 orbits, shown as a function of the TOMS swath position. The error bars are estimated from the standard deviation computed from the 90 orbits. The correction is subtracted from the measured N_{340}-value.

4. Error analysis

4.1. Random errors and SO_2 detection limit.

The random errors in the MS_SO2 retrieval were estimated from the standard deviation in the SO_2 from a large data sample that included 90 central Pacific orbits, spanning a ten-year period between 1980 and 1990. Data were restricted to Σ values between -20 and 20 DU (Fig. 7a). Standard deviations were then computed as a function of the TOMS swath position as shown in Fig. 7b. Figure 7b can be used to characterize the SO_2 detection limits for TOMS. In this section, we compare the TOMS error distribution with the UV Ozone Mapping Profile Suite Nadir Mapper (OMPS-NM), a hyperspectral UV instrument on board the Suomi National Polar-orbiting Partnership (NPP) and NOAA 20 satellites. For this comparison, we selected one month of NPP/OMPS spectral data (central Pacific) and applied the MS_SO2 algorithm using the same four wavelength bands on TOMS (Table 2), which were first convolved with the TOMS bandpass function.

Figure 7b shows that TOMS retrieval noise depends on the swath position, varying from ~ 6 DU at nadir to ~4 DU at higher viewing angles, while OMPS is 2-3 times smaller (~2 DU) and is relatively independent of the cross-track position (Figure 7). Using the MS_SO2 algorithm, we subsequently estimate the SO2 detection limit for TOMS and OMPS-NM to be about 15 DU and 6 DU (~99% confidence level), respectively. We note that applying the Principal Component Algorithm (PCA) (Li et al., 2013) to all the 100-200 wavelengths available from OMPS-NM hyperspectral measurements, the noise spectrum is reduced by an order of magnitude to ~0.2-0.5DU (Zhang et al., 2017), allowing detection of large anthropogenic points sources (emissions more than ~80 kt yr^{-1}) (Fioletov et al., 2016).
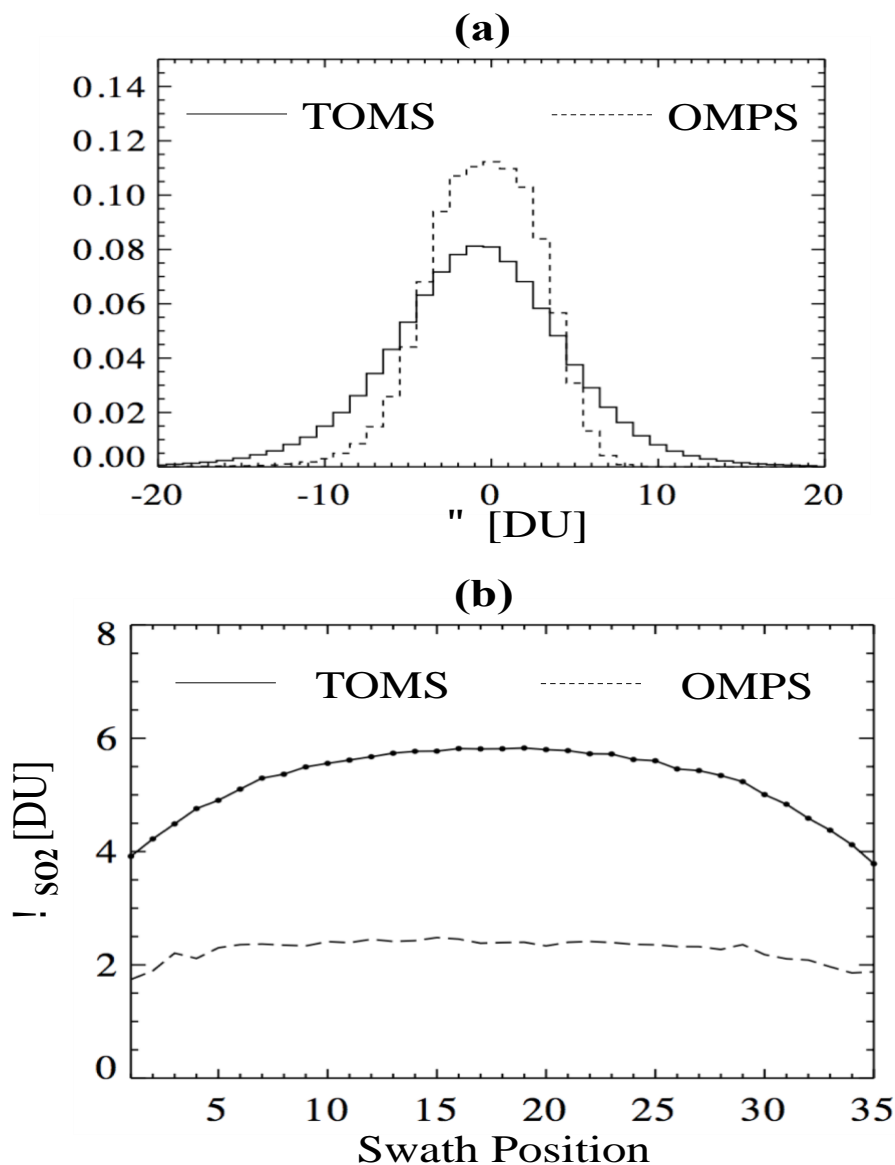
16

Figure 7. (a) Background retrieved SO$_2$ noise histogram for Nimbus-7 TOMS (solid line) and current operational hyperspectral Ozone Mapping Profiling Suite (OMPS) nadir mapper (dashed line) for all swath positions; (b) Noise standard deviations of background SO$_2$ retrievals as a function of the swath position. OMPS noise is factor of 2-3 less than TOMS and less dependent on cross-track position.

4.2 Systematic errors in volcanic SO₂ plumes

In this section, we evaluate systematic errors of the MS_SO2 retrievals of volcanic SO_2. The two most significant errors are caused by volcanic aerosols (ash and sulfate) and incorrect assumptions
5   regarding the SO_2 profile, namely the plume height. The radiance LUTs used by the algorithm account for ozone and SO_2 absorption, but do not account for the absorption and scattering by aerosols. The ash errors can be significant during the first couple days after the initial eruption phase (Rose et al., 2003, Guo et al., 2004). The pre-computed radiance tables used by MS_SO2 assume an SO_2 column amount based on an a priori CMA and standard deviation (Section 3). An incorrect CMA assumption can cause
10   significant SO_2 errors that vary with viewing geometry, ozone and SO_2 column amounts. We characterize these errors by applying the MS_SO2 algorithm to synthetic radiances.

4.2.1 Uncertainties due to SO₂ plume height

To understand retrieval errors in MS_SO2 algorithm due to assumed a priori SO_2 profiles, we calculated column SO_2 Jacobians $\partial N / \partial \Omega_{SO_2}$ using the VLIDORT radiative transfer code (Spurr and
15   Christi 2019) for the typical observational conditions in the tropics, mid latitudes, and high latitudes. Figure 8 shows $\partial N / \partial \Omega_{SO_2}$ at 317 nm, for different SO_2 amounts, nadir angles and scene reflectance as function of the assumed SO_2 height (center of mass altitude, CMA). The Jacobians generally increase with the CMA, meaning that satellite BUV measurements are more sensitive to SO_2 at higher altitudes. This means that the MS_SO2 algorithm will overestimate (underestimate) the SO_2 column amount, if
20   the CMA of the a priori profile is lower (higher) than that of the actual SO_2 profile. On the other hand, the sensitivity of SO_2 Jacobians with respect to CMA is affected by several factors, particularly SO_2 column amounts, geometry (solar zenith angle and viewing zenith angle), the reflectivity of the underlying surface (Rs), and the CMA itself. In general, the sensitivity of SO_2 Jacobians to CMA is greater for SO_2 plumes with large SO_2 loading (e.g., 300 DU *vs.* 50 DU), at relatively low altitudes
25   (e.g., CMA of 13 km *vs.* 18 km), and for lower reflectivity (e.g., Rs of 0.05 *vs.* 0.50) or are near the edge of the swath (e.g., VZA of 60° *vs.* 0°). For calculations assuming typical mid- and high-latitude conditions, we found similar sensitivities of SO_2 Jacobians to CMA. From these calculations, we can estimate the errors in the SO_2 Jacobians at 317 nm, assuming that the standard a priori profiles used in MS_SO2 retrievals (CMA: 13 and 18 km) have a ±2 km error in CMA. The results for the tropics, mid
30   latitudes, and high latitudes are summarized in the supplement Tables S1, S2, and S3, respectively. As shown in the tables, for SO_2 plumes from relatively moderate eruptions (~50 DU), the relative errors in SO_2 Jacobians due to the error in the CMA are mostly within ±10%. But for plumes with large SO_2

Atmospheric
Measurement
Techniques
Discussions
Open Access
EGU

loading (~200-300 DU) from explosive eruptions such as Pinatubo, the relative error in SO_2 Jacobians may reach as high as 30% for pixels near the edge of swath that have low reflectivity. Additionally, for pixels with the same reflectivity and VZA, the relative errors due to SO_2 height are greater for mid- and high-latitude eruptions than for tropical eruptions.

5   To quantify the retrieval errors due to inaccuracies in the a priori profiles, we used the top-of-the-atmosphere synthetic radiance data generated by VLIDORT, as input to the MS_SO2 algorithm. The retrieved SO_2 and O_3 column amounts were compared with assumed in VLIDORT calculations (Tables S4-S7 in the supplement). As shown in the tables, for SO_2 plumes with a modest loading (~50 DU), the relative errors in SO_2 column amounts, due to a 2-km error in the *a priori* profile are typically 10   10% or less, whereas the relative errors in O_3 are within 1%. For plumes with large SO_2 loadings (200-300 DU), the errors in SO_2 amounts due to a 2-km bias in the *a priori* profile are typically 5-15%, but can reach as high as 30-40% for high latitude plumes with large SZA and VZA. For extreme conditions at high latitudes (Table S5, 13 km *a priori* profile *vs.* 15 km actual profile, SO_2=300 DU, VZA=60°), the MS_SO2 algorithm failed to converge after 20 iterations, due to a signal saturation caused by strong 15   absorption at 317 nm. In these relatively rare cases, it is beneficial to use longer wavelengths (e.g., > 320 nm) for SO_2 retrievals (e.g., Li et al., 2017; Theys et al., 2015), which are available from the current hyperspectral instruments such as OMI and OMPS, but not TOMS.

    We also calculated the diagnostic residual at 312 nm ($res_{312} = N_{meas} - N_{calc}$), defined here as the difference between the "measured" synthetic N_{meas} and the N_{calc} at 312nm using MS_SO2 retrieved 20   ozone and SO_2 column amounts. Note that the 312 nm channel was not used in the MS_SO2 algorithm, and the residuals at other wavelengths are essentially zero since we are retrieving four parameters from four wavelengths. As shown in the Supplement Tables S4-S7, a positive bias in the SO_2 height (CMA too high as compared with the actual profile) leads to negative residuals at 312 nm, whereas a negative bias in *a priori* profile (CMA too low) causes positive residuals. The residuals are generally within 1-2 25 N value (2% -5% error in radiance) for SO_2 column amounts of 50-100 DU, but can reach 3-7 N value (6% -15%) for large SO_2 amounts of 200-300 DU. While the 312 nm channel may potentially be used to retrieve SO_2 plume height for large volcanic eruptions, it is also strongly affected by volcanic aerosols as demonstrated in the next section.
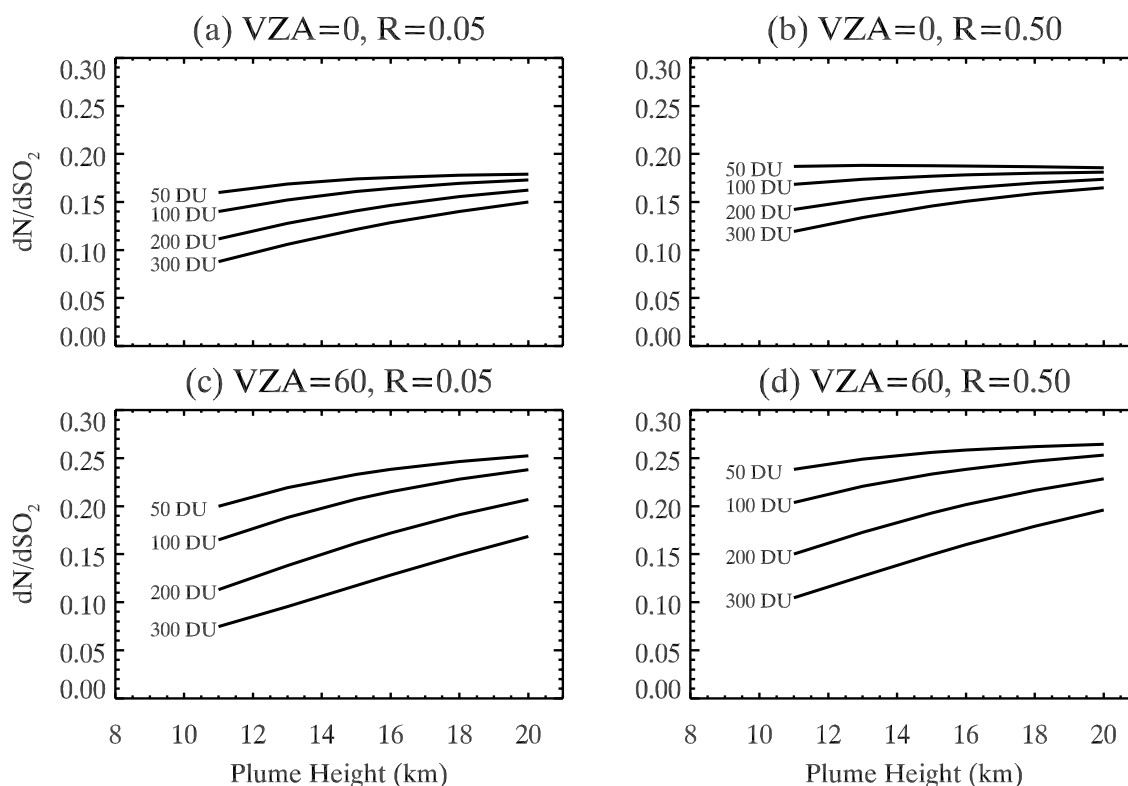
Atmospheric
Measurement
Techniques
Discussions

Open Access

Figure 8. VLIDORT calculated SO_2 column Jacobians ($\partial N / \partial SO_2$) at 317 nm for typical conditions in the tropics (SZA=10°, RAZ=90°, $O_3 = 275$ DU) but different SO_2 column amounts (50, 100, 200, and 300 DU), center mass altitudes (11-20 km), viewing zenith angle (VZA = 0° and 60°), and SLER (R = 0.05 and 0.50). For these calculations, Gaussian SO_2 profiles with the same standard deviation (2 km) were assumed.

4.2.2 Ash and sulfate aerosol effects on MS_SO2 retrievals

To test the sensitivity of the MS_SO2 algorithm to ash and sulfate aerosols, an Observing System Simulation Experiment (OSSE) was conducted. The experiment used the GEOS-5 earth system model (*Molod et al., 2012, Buchard et al., 2017, Colarco, et al, 2012*), coupled with the online Goddard Chemistry Aerosol and Radiation (GOCART) (*Chin et al., 2000; Colarco et al., 2010, and references therein*) and the Community Aerosol and Radiation Model for Atmospheres (CARMA) (*Toon et al. 1988; Ackerman et al. 1995; Colarco et al., 2014*). In this experiment, we considered three separate cases for a Pinatubo-like eruption scenario: 1) 12 Mt of SO_2 and no aerosols; 2) 12 Mt of SO_2 plus 4 MT of sulfate aerosols (as reported by Guo et al. ,2004) and 3) 12 Mt of SO_2, 4 Mt of sulfate aerosols

Atmospheric
Measurement
Techniques
Open Access
Discussions
EGU

plus 5 Mt of ash uniformly distributed between 18 km and 22km above the location of Pinatubo volcano, on June 15, 1991, from 06:00 – 15:00 UTC.

The GEOS-5 simulated 4D profiles of ozone, SO_2, sulfate aerosols, and volcanic ash were used as input to a VLIDORT RT model (Spurr and Christi 2019). The model generated synthetic radiances at 5   317, 331, 340 and 380 nm TOMS bands, using the actual SNPP/OMPS-NM viewing geometry, and assuming cloud-free conditions. The synthetic radiances produced by the VLIDORT were used as input to the MS_SO2 algorithm to generate "retrieved" columns of ozone and SO_2. We note that MS_SO2 algorithm uses LUTs produced using a different TOMRAD RT model (Dave 1964).

Figure 9 compares retrieved versus true SO_2 column amounts for the three cases considered. The 10   retrieval bias is inferred from the differences between the model SO_2 input and the SO_2 retrieved by MS_SO2, using the radiances from the model run. The no aerosol case confirms an unbiased SO_2 retrievals for SO_2 column amounts less than ~150 DU and small positive bias for larger SO_2 amounts. For aerosol cases where sulfates and ash were included in the simulation, we observe a negative bias for SO_2 column amounts exceeding ~100 DU. These negative biases (retrieval minus input) are expected as 15   the MS_SO2 forward model does not explicitly account for volcanic aerosols. This OSSE experiment shows the effects of heavy aerosol loading on the retrieval, but also increases confidence in MS_SO2 retrievals between 15-100 DU, under nominal conditions, even in the presence of high aerosol concentrations.
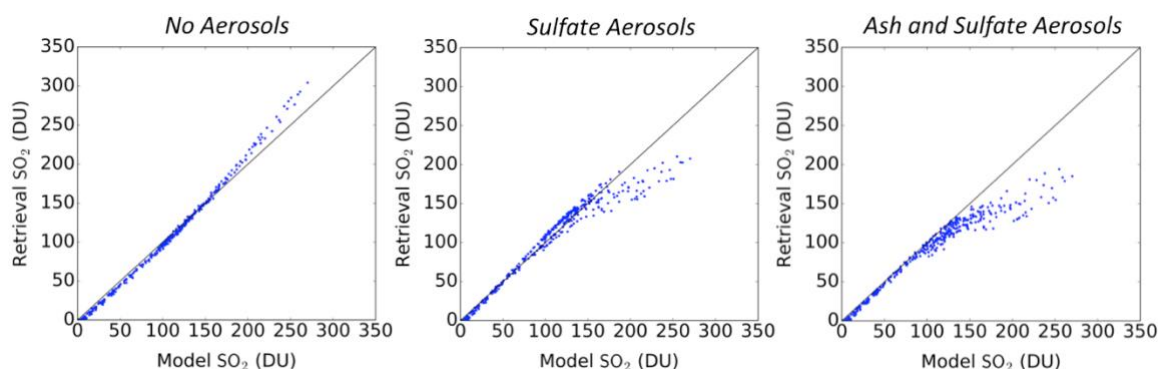

20

Figure 9. Comparison of the OMPS retrieval SO_2 against the GEOS-5 model SO_2. The TOA radiances for the OMPS retrieval were generated assuming no aerosol (left panel), only non-absorbing sulfate aerosols (center panel), and both ash and sulfate aerosols (right panel).

Atmospheric
Measurement
Techniques
Discussions

5 Comparison with PCA SO₂ retrievals

We validated the algorithm by directly comparing MS_SO2 retrievals with the independent principal component analysis (PCA) SO₂ algorithm adapted to the TOMS 6 spectral channels. In the PCA approach (Li et al., 2013; 2017), a set of principal components (PCs) is first extracted from the
5   measured radiances using a PCA technique and ranked in descending order according to the spectral variance they each explain. If derived from SO₂-free areas, these PCs represent geophysical processes (*e.g.*, ozone absorption) and measurement details (*e.g.*, wavelength shift) that are unrelated to SO₂, but may interfere with SO₂ retrievals. Next, we fit the first n_v (non-SO₂) PCs and the SO₂ Jacobians ($\partial N/\partial \Omega_{SO_2}$) to the measured radiances (in N value) described in Eq. (11). This allows us to
10 simultaneously estimate the coefficients of the PCs (ω) and SO₂ column amount (Ω_{SO2}), and helps to minimize the impacts of various interfering processes:

$$N(\omega, SO_2) = \sum_{i=1}^{n_v} \omega_i v_i + \Omega_{SO_2} \frac{\partial N}{\partial SO_2} N. \qquad (11)$$

A more detailed introduction to the PCA SO₂ retrieval technique for hyperspectral instruments such as the Ozone Monitoring Instrument (OMI) and the Ozone Mapping and Profiler Suite Nadir
15 Mapper (OMPS-NM) can be found elsewhere (e.g., Li et al., 2013, 2017; Zhang et al., 2017).

For this comparison we adapt the PCA to discrete wavelength of N7/TOMS. The Nimbus-7 TOMS PCA SO₂ algorithm is similar to the OMI and OMPS-NM version in terms of its overall structure but differs in some implementation details. Specifically, unlike the OMI/OMPS volcanic SO₂ retrievals that use a dynamic spectral fitting window (Li et al., 2017), the TOMS PCA SO₂ algorithm
20 uses all six wavelengths available from TOMS in fitting. Also due to the small number of wavelengths, in the TOMS PCA SO₂ algorithm, we always use $n_v = 5$ PCs in Eq. (11), less than the number of PCs used for OMI ($n_v \leq 20$) or OMPS ($n_v \leq 15$). For OMI and OMPS retrievals, SLER is derived at three wavelengths (342, 354, and 367 nm) and extrapolated to other wavelengths using a second-degree polynomial function fitted to these three wavelengths. As for TOMS, SLER is determined at 340 and
25 380 nm and extrapolated linearly. Additionally, while the Jacobians lookup tables are constructed using the VLIDORT radiative transfer code (Spurr and Christi 2019) for both OMI/OMPS and Nimbus-7 TOMS, different, instrument-specific slit functions are used to band-pass the SO₂ Jacobians from the lookup tables.

We compared retrievals from the two algorithms for the first six days of Mount Pinatubo
30 eruption (June 16-21, 1991). The Pinatubo case provides a large sample of FoVs spanning a broad range of SO₂ amounts from 15 DU (minimum threshold) to over 400 DU. In this test of the algorithm, MS_SO2 and PCA retrievals were generated assuming a CMA =18 km.

Atmospheric
Measurement
Techniques
Open Access
Discussions
EGU

5.1 June 1991 eruption of Mount Pinatubo

Mount Pinatubo is a large stratovolcano located at 15°08' N,120°21'E in western Luzon, Philippines, that erupted explosively on June 15, 1991, following weeks of precursory activity. TOMS SO_2 imagery on June 15 shows a narrow, elongated SO_2-ash plume extending to the west from the
5   location of the volcano. On the following day TOMS measured a massive SO_2 plume to the west of the volcano (Bluth et al., 1992). TOMS continued tracking the daily evolution of the Pinatubo volcanic cloud as it encircled the earth over a period of about 22 days. Previous estimates of the Pinatubo SO_2 height (CMA) range between 18 and 25 km (Self et al., 1994; Guo et al., 2004).

Figure 10 shows TOMS daily SO_2 maps produced with the MS_SO2 and the PCA algorithms
10 for the six-day period from June 16 to June 21. Corresponding Ash Index (AI) imagery from MS_SO2 are shown in Figure 11. The SO_2 and AI maps for June 16 show a large SO_2 and ash cloud propagating to the west. The AI values range from 4 to above ~10 across the cloud. The AI values decreased over the following days due to wind advection and wet deposition (Guo et al., 2004). As the SO_2 cloud area continues to expand, total SO_2 mass remain high, while SO_2 peak values decrease, which is expected
15 from the cloud dispersion. The MS_SO2 and the PCA imagery show excellent qualitative agreement in the total cloud area and internal SO_2 plume structure, as inferred from the SO_2 gradients across the peak regions of the cloud. Note that for June 16-19, part of the observed cloud is missing due to a known mechanical problem with the TOMS instrument. These missing regions can be clearly identified in the imagery.

20 Figure 12 shows a scatterplot comparing the MS_SO2 and PCA retrievals for the 6-day time series, which included over 7000 matching FoVs. These results show the retrievals are in close quantitative agreement, with a correlation of 0.993 and a unit slope. Since the two algorithms apply fundamentally different approaches to retrieving SO_2, this level of agreement is impressive considered over such a broad range of values.

25 We further compared quantitative retrievals of the total SO_2 cloud mass, peak SO_2 values and the cloud area. For this comparison, we also considered results from the Krueger-Kerr algorithm (KK), based on the published results of Guo et al. (2004). Table 3 displays daily estimates of the SO_2 cloud mass and peak SO_2 amounts for the MS_SO2, PCA and KK algorithms for the six-day period. Guo et al. (2004) applied a modified version of the KK algorithm that assumes a radiative transfer air mass
30 factor (AMF), which accounts for the a priori ozone and SO_2 absorption profiles (Krotkov et al., 1997). The early SO_2 mass estimates by Bluth (1992) derived from Pinatubo eruption assumed a simplified geometrical AMF. Also note that Guo et al. (2004) interpolated across the missing data regions of the plume on June 16, June 18 and June 19 using a Punctual Kriging statistical analysis. Here, we did not correct for the missing data. The three algorithms are in good overall agreement for the period from

Atmospheric
Measurement
Techniques
Discussions

June 17 to June 21, with the differences within 10% compared to MS_SO2. The most significant differences between the three algorithms are observed on June 16 under conditions of heavy ash loading. The KK SO₂ mass exceeded MS_SO2 by over ~20%, while the MS_SO2 and the PCA mass retrievals differ by just 2%. Some of the difference between KK and the other two algorithms can be attributed to the fact that the Guo et al. (2004) estimates include contribution from the missing data region at the northern boundary of the plume (compare SO_2 and aerosol imagery), but this contribution does not nearly account for the total difference in Table 3.

The differences can be explained by considering how each algorithm are affected by volcanic aerosols. The MS_SO2 accounts for ash implicitly by retrieving the LER spectral dependence at 340 nm, which is then used iteratively to correct the LER at the two absorbing channels. As explained in Sec. 3.2, absorbing aerosols cause possible apparent retrieved ozone increase, which decrease Σ. The KK algorithm (Krueger et al., 1995) also accounts for ash implicitly by retrieving two linear spectral parameters a and b that adjust to match N_{calc} and N_{meas} for all spectral channels, including the shortest 312nm. The KK radiative path LUTs are based on TOMRAD calculations that do not explicitly account for ash (Krotkov et al., 1997). Krueger et al. (1995) estimated that ash aerosols can cause errors in the retrieval up to +30%, depending on the ash size distribution. The measurements driven PCA algorithm, in contrast, accounts for ash empirically by separation and ordering of the measured spectral principal vectors. The differences between MS_SO2 and KK on June 16 and June 17 can be partly ascribed to the effects of aerosols on the retrievals.

By June 18, the ash and SO_2 clouds have mostly separated, though, aerosol indices over 4 are still observed in some regions of the plume. Pinatubo did not erupt again after the major eruption on June 15, yet the three algorithms show retrieved SO_2 mass increases on June 17 and June 20 (the PCA and KK retrievals also indicate a small increase on June 18). Guo et al. (2004) attribute these increases to the sequestering of volcanic SO_2 by ice-ash mixtures in the cloud. They propose the sequestered SO_2 was released at a later time through sublimation of ice in the lower stratosphere. The oxidation of hydrogen sulfide offers another mechanism to account for the observed SO_2 mass increases in the first few days following the eruption. The combined results of the three algorithms support the conclusions of Guo et al., (2006) that the observed SO_2 mass increases in the temporal evolution of the plume are real.

Overall, the PCA retrieved ~3% more total SO_2 mass than MS_SO2. These differences are attributed to differences in how the algorithms handle aerosols and the differences in the calculated area of the SO_2 cloud due to the differences in the SO_2 values near the sensitivity threshold (~15 DU). Ash, sulfates and high SO_2 amounts impact the ozone retrieval, for as was seen in 3.2, systematic errors in SO_2 are anticorrelated with errors in O_3 (see Fig. S1). For the case of the KK algorithm, the total ozone

24

retrieved inside the SO₂ plume can be unrealistically low, and even negative in an extreme event like
Mt. Pinatubo shown in Figures S3 and S4 of the supplement. The Figure S3 compares the KK ozone
retrieval with MS_SO2 step 2 ozone retrieval and the Figure S4 compares scatterplots of SO₂ and total
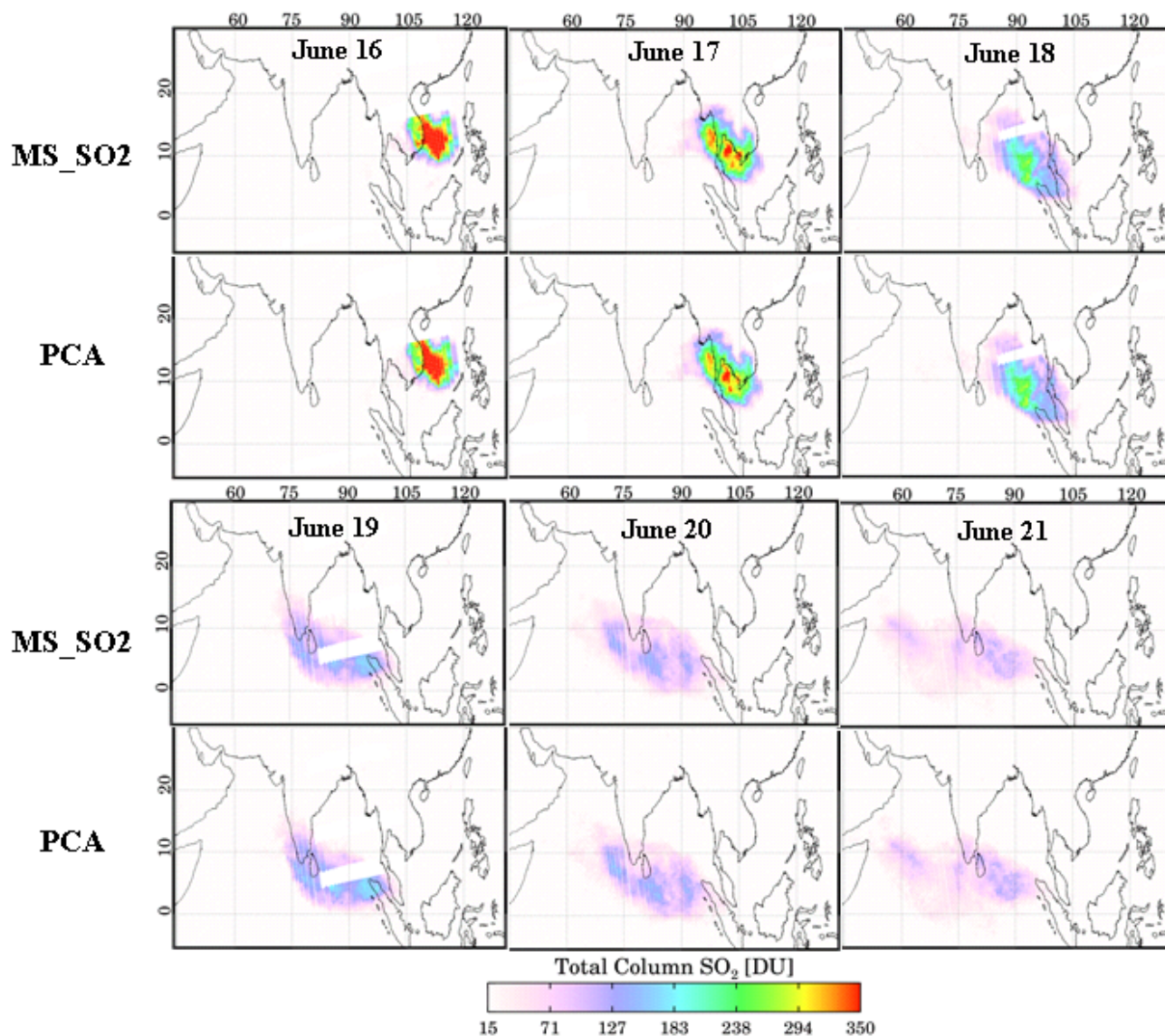ozone for June 17 and June 18.

Figure 10. Daily SO₂ maps retrieved during Nimbus7 TOMS overpasses of the Pinatubo
eruption cloud between June 15 and June 21, 1991, show excellent agreement between the two
independent MS_SO2 and PCA retrieval algorithms.

Table 4 compared estimates of the SO$_2$ cloud area for the MS_SO2 and PCA retrievals. The area is most sensitive to the minimum detection threshold around the edges of the SO$_2$ cloud. The MS_SO2 and the PCA algorithms were directly compared by computing the sum of all the pixels where $\Sigma > 15$ DU (Fig. 10). For the six-day study period, the plume increased in size from about a little over 2 x 10^6 km^2 to ~9 x 10^6 km^2. The PCA retrieval observed a larger cloud area for the five of the six days, but the observed differences were within 10%. On June 16, shortly after the major eruption of June 15, the PCA estimated area for the SO$_2$ cloud is about ~15% greater than that retrieved using the MS_SO2 algorithm. The fresh plumes are opaque, which result in underestimating of SO$_2$ mass by all BUV algorithms due to the mixing of water, ice and aerosols (Krotkov et al., 1997). The PCA retrieval appears more sensitive to SO$_2$ near the edges of the cloud, where the ash aerosol loading is high (AI > 1.5). It should be noted that the soft calibration applied to the 340 nm channel, described in 3.3, may also contribute to the lowering the sensitivity around the edges of the plume. This correction effectively lowered the background SO$_2$ by about 3 DU.
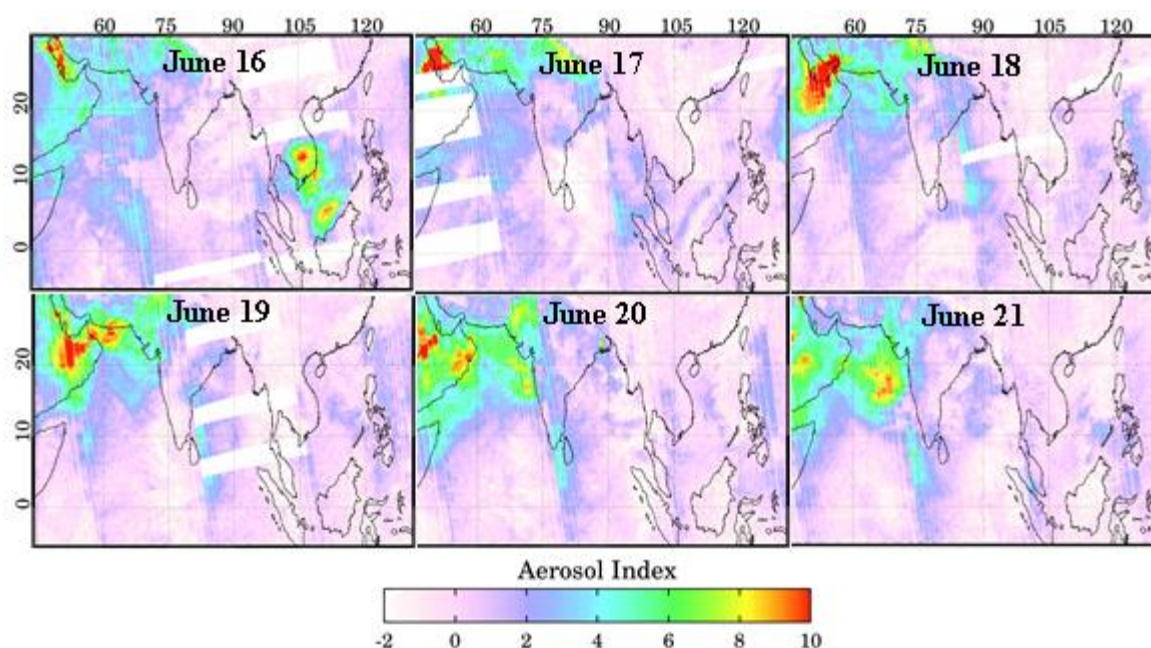

Figure 11. Daily Aerosol Index (AI) imagery retrieved using MS_SO2 between June 16 and June 21, 1991. Positive AI values over India and Arabia peninsula are due to dust aerosols, not related to the Pinatubo ash cloud.
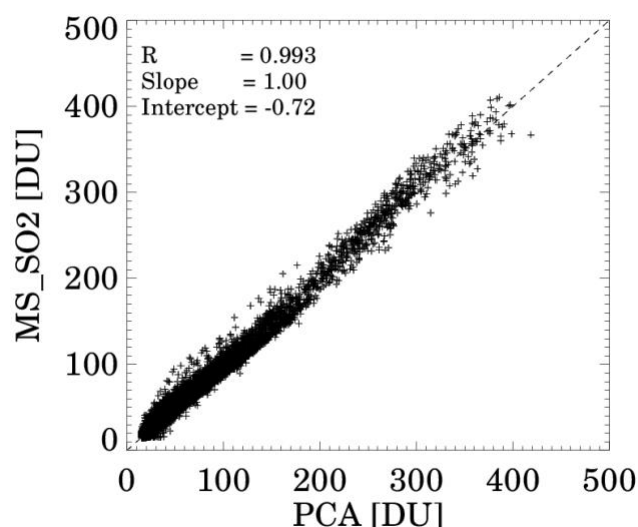
Atmospheric
Measurement
Techniques
Discussions

Figure 12. Scatterplot of retrieved SO₂ (Dobson Units) using PCA and MS_SO2 algorithms for the period June 15-21, 1991.

Table 3: Daily SO₂ mass and maximal SO₂ values for MS_SO2, PCA and KK (Guo et al., 2004) algorithms for the five days following the Pinatubo eruption on June 15, 1991.

Day in June 1991	MS_SO2 algorithm		PCA algorithm		Krueger_Kerr Algorithm		Percent Difference (%)	
	SO₂ Mass (kt)	Max SO₂ (DU)	SO₂ Mass (kt)	Max SO₂ (DU)	SO₂ Mass (kt)	Max SO₂ (DU)	PCA	KK
06/16	9.8	410	10.0	418	12.0*	537	-2.0	24.3
06/17	12.1	389	12.1	399	13.0	423	0.0	7.4
06/18	12.0	279	12.4	280	13.1*	350	3.3	9.2
06/19	10.9	173	11.6	180	11.4*	207	6.2	4.6
06/20	12.6	148	13.2	157	12.2	180	4.7	-4.0
06/21	11.8	125	12.5	130	11.9	137	5.9	0.8

* Guo et al.,(2004) interpolated values in the missing data region seen in maps for June 16, 18, and 19

Table 4: SO$_2$ plume area and the number of FoVs where the retrieved SO$_2$ exceeded 15 DU for the MS_SO2, PCA and KK algorithms for the five days following for the Pinatubo eruption on June 15, 1991.

Day	MS_SO2		PCA		Percent Difference (%)
	Area (x10^6 km^2)	NFovs (Σ>15 DU)	Area (x10^6 km^2)	NFovs (Σ>15 DU)	PCA
06/16	2.13	442	2.48	519	15.2
06/17	4.19	1006	4.04	971	-3.6
06/18	5.05	1062	5.31	1088	5.0
06/19	5.09	910	5.30	957	4.0
06/20	7.27	1407	7.59	1487	4.3
06/21	8.44	1674	9.02	1805	6.6

6 Conclusions

This paper describes, a multi-satellite, multi-spectral UV algorithm (MS_SO2) for retrieving volcanic SO$_2$ that was used operationally to re-process measurements from the heritage Nimbus-7 TOMS and the current Deep Space Climate Observatory Earth Polychromatic Imaging Camera (Carn et al., 2018; Marshak et al., 2018). The MS_SO2 algorithm can process data from current hyperspectral UV spectrometers, such as SNPP/OMPS and Aura/OMI, using a convolved, discrete set of wavelengths, offering a viable means for intercomparing volcanic SO$_2$ retrievals from different missions.

We estimated random (noise) and systematic errors, related to the effects of volcanic aerosols and uncertainties in SO$_2$ height and partly corrected for absorbing ash, using positive aerosol index (AI) as a proxy for applying a Step 2 correction to the SO$_2$ retrievals. The correction could still underestimate SO$_2$ mass during the first days after extremely large eruptions (VEI > 3) due to BUV saturation. In such cases we recommend estimating e-folding time of the SO$_2$ conversion to sulfate aerosols, using later measurements and extrapolating SO$_2$ mass exponentially back in time to the eruption day (Krotkov et al., 2010).

The TOMS observational System Simulation Experiment (OSSE) confirmed unbiased SO_2 retrievals using synthetic radiances for $SO_2 < 100\text{-}150$ DU, but low biases for larger SO_2 amounts due to the presence of ash and sulfate aerosols. Therefore, operational MS_SO2 retrievals should provide a low boundary constraint on the SO_2 mass injected into the atmosphere from large eruptions. The

5 algorithm can be further improved by explicitly accounting for volcanic ash and sulfate aerosols, which was not feasible in the operational re-processing.

The MS_SO2 retrieval is also sensitive to the differences between the a priori and actual SO_2 center of mass altitude. Since this key parameter is not retrieved, the TOMS SO_2 product provides separate SO_2 column amounts assuming three different altitudes (8, 13 and 18 km). Users should select

10 one SO_2 column amount that is most appropriate for a particular eruption.

To validate the accuracy of the TOMS SO_2 retrievals, we compared the MS_SO2 with the independent measurements-bbased Principal Component Analysis (PCA) algorithm for the first six days following the 1991 Pinatubo eruption. The daily time series of the SO_2 retrievals show high correlation ($R^2 =0.986$) and unbiased agreement between the two retrievals over a broad SO_2 range between 15 DU

15 and 400 DU. We also compared the total SO_2 mass, peak SO_2 amounts and plume area with the heritage KK algorithm. This 3-way comparison showed the SO_2 mass within 10% for all days, except on June 16, when the Krueger-Kerr algorithm retrieved 24% higher SO_2 mass. This could be explained by interpolation over a region of missing TOMS measurements on June 16 (Guo et al., 2004). The remaining differences between the MS_SO2 and the PCA algorithms (3-7%) are attributed to the

20 differences in handling of aerosols, and different sensitivity thresholds of the algorithms.

The re-processed Nimbus-7 TOMS volcanic SO_2 data set, TOMSN7SO2 (Krotkov et al., 2017) is now publicly available through the Goddard Earth Sciences Data and Information Services Center (GES DISC) as part of the NASA's Making Earth System Data Records for Use in Research Environments (MEaSUREs) program at https://doi.org/10.5067/MEASURES/SO2/DATA202. We plan

25 to reprocess all follow-up multi-spectral UV (TOMS) and hyperspectral UV (OMI, OMPS) missions (Figure 1) with MS_SO2 and PCA algorithms to keep updating our multi-satellite volcanic SO_2 mass database (MSVOLSO2L4) archived at GES DISC (Carn 2019). It is important to continue quantifying SO_2 emissions from small explosive eruptions, as they may, collectively, play an important role in sustaining the persistent, background stratospheric aerosol layer, which is an important factor in global

30 climate forcing.

Atmospheric
Measurement
Techniques
Discussions

References

Ahmad, Z. and P. K. Bhartia: Effect of Molecular anisotropy on the backscattered UV radiance, *Appl. Opt.*, **34**, 8309-8314, https://doi.org/10.1364/AO.34.008309, 1995.

Ahmad, Z. P. K. Bhartia and N. Krotkov: Spectral properties of backscattered UV radiation in cloudy
5   atmospheres, *J. Geophys. Res. Atmos.*, 109, D01201, https://doi.org/10.1029/2003JD003395, 2004.

Bhartia, P.K., J.Herman, R.D.McPeters, and O.Torres: Effect of Mount Pinatubo aerosols on total ozone measurements from back-scattered ultraviolet (BUV) experiments, *J. Geophys. Res.*, **98**, 18547-18554, http://doi.org/10.1029/93JD01739, 1993.

Bobrowski, N. G. Honninger, B. Galle, and U. Platt: Detection of bromine monoxide in a volcanic
10 plume, *Nature*, 423, http://doi:10.1038/nature01625, 2003.

Bogumil, K., J. Orphal, T. Homann, S. Voigt, P. Spietz, O.C. Fleischmann, A. Vogel, M. Hartmann, H. Kromminga, H. Bovensmann, J. Frerick, J.P. Burrows (2003): Measurements of molecular absorption spectra with the SCIAMACHY pre-flight model: instrument characterization and reference data for atmospheric remote-sensing in the 230-2380 nm region, *J. of Photochem. and Photobiology*, *A*:, 157,
15 167-184, https://doi.org/10.1016/S1010-6030(03)00062-5, 2003.

Bluth, J. S. G., S. D. Doiron, C. C. Schnetzler, A. J. Krueger, L. S. Walter: Global tracking of the SO2 clouds from the June, 1991 Mount Pinatubo eruptions, *Geophys. Res. Lett.*, 151-154, https://doi.org/10.1029/91GL02792, 1992.

Buchard, V., C. A. Randles, A. da Silva,A. S. Darmenov, P. R. Colarco,R. C. Govindaraju, R. A.
20 Ferrare, J. W. Hair, A. Beyersdorf, L. D. Ziemba, and H. Yu: The MERRA-2 Aerosol Reanalysis, 1980-onward, Part II: Evaluation and Case Studies. *J. Clim*, 30, 6851-6872. DOI: 10.1175/JCLI-D-16-0613.1, 2017.

Carn, S.A., Krueger, A.J., Bluth, G.J.S., Schaefer, S.J., Krotkov, N.A., Watson, I.M. and Datta, S.: Volcanic eruption detection by the Total Ozone Mapping Spectrometer (TOMS) instruments: a 22-year
25 record of sulfur dioxide and ash emissions, In: Volcanic Degassing (eds. C. Oppenheimer, D.M. Pyle and J. Barclay), *Geological Society, London, Special Publications*, **213**, 177-202, https://doi.org/10.1144/GSL.SP.2003.213.01.11, 2003.

Carn, S.A., Yang, K., Prata, A.J., Krotkov, N.A.: Extending the long-term record of volcanic SO_2 emissions with the Ozone Mapping and Profiler Suite (OMPS) Nadir Mapper, Geophys. Res. Lett. 42.
30 http://doi.org/10.1002/2014GL062437, 2015.

Carn, S.A., L. Clarisse and A.J. Prata: Multi-decadal satellite measurements of global volcanic degassing, *J. Volcanol. Geotherm. Res*., 311, 99-134, http://doi.org/10.1016/j.jvolgeores.2016.01.002, 2016.

Atmospheric
Measurement
Techniques
Open Access
EGU
Discussions

Carn. S. A., Multi-Satellite Volcanic Sulfur Dioxide L4 Long-Term Global Database V3, Greenbelt, MD, USA, Goddard Earth Science Data and Information Services Center (GES DISC), Accessed: May 10 2019, doi: 10.5067/MEASURES/SO2/DATA404, 2019

Colarco, P. R., S. Gasso, C. Ahn, V. Buchard, A. M. da Silva, and O. Torres: Simulation of the Ozone
5   Monitoring Instrument aerosol index using the NASA Goddard Earth Observing System aerosol reanalysis products. *Atmos. Meas.Tech.*, 10, 11, 4121-4134. DOI: 10.5194/amt-10-4121-2017, 2017.

Daumont, M., Brion, J., Charbonnier, J., and Malicet, J.: Ozone UV spectroscopy I: Absorption cross-sections at room temperature, *J. Atmos. Chem.*, **15**, 145–155, https://doi.org/10.1016/j.jvolgeores.2016.01.002, 1992.

10   Dave, J. D.: Meaning of successive iteration of the auxiliary equation in the theory of radiative transfer, *Astrophys. J.*, **140**, 1292-1303, https://doi.org/10.1086/148024, 1964.

Dave, J. V., and C. L. Mateer: A preliminary study on the possibility of estimating total atmospheric ozone from satellite measurements, *J. Atmos. Sci.*, **24**, 414-427, https://doi.org/10.1175/1520-0469(1967)024<0414:APSOTP>2.0.CO;2, 1967.

15   Guo, S., G. J. S. Bluth, W. I. Rose, I. M. Watson, A. J. Prata: Revaluation of SO2 release of the 15 June 1991 Pinatubo eruption using ultraviolet and infrared satellite sensors. *Geochem, Geophys, Geosys.*, **5**, 1-31, Q04001, http://doi.org/10.1029/ 2003GC000654, 2004.

Joiner, J., P. K. Bhartia, R. P.Cebula, E. Hilsenrath, R. D. McPeters, and H. W. Park: Rotational-Raman Scattering (Ring Effect) in satellite backscatter ultraviolet measurements, *Appl. Opt.,* 34, 4513-4525,
20   https://doi.org/10.1364/AO.34.004513, 1995.

Kerr, J.B., C.T. EcElroy, and R. A. Olafson: Measurements of ozone with the Brewer ozone spectrophotometer, *Proc. Int. Ozone Symp.*, 1, 74-79, https://doi.org/10.1029/94JD02147, 1980.

Khokhar, M.F., Frankenberg, C., Van Roozendael, M., Beirle, S., Kühl, S., Richter, A., Platt, U., Wagner, T.: Satellite observations of atmospheric SO2 from volcanic eruptions during the time-period
25   of 1996–2002, Adv. Space Res. 36, 879–887. http://doi. org/10.1016/j.asr.2005.04.114, 2002.

Klobas, J. E., D. M. Wilmouth, D. K. Weisenstein, J. G. Anderson, and R. J. Salawitch: Ozone depletion following future volcanic eruptions, *Geophys. Res. Lett.*, **44**, 7490–7499, https://doi.org/10.1002/2017GL073972, 2017.

Krotkov, N. A., A. J. Krueger and P. K. Bhartia: Ultraviolet optical model of volcanic clouds for remote
30   sensing of ash and sulfur dioxide, *J. Geophys. Res.*, **102**, 21891-21904, https://doi.org/10.1029/97JD01690, 1997.

Krotkov N.A., M. Schoeberl, G. Morris, S. Carn, and Kai Yang, Dispersion and lifetime of the SO2 cloud from the August 2008 Kasatochi eruption, *J. Geophysical Research*, 115, D00L20, doi:10.1029/2010JD013984, 2010.

Atmospheric
Measurement
Techniques
Discussions

Krotkov, N. A., Pawan K. Bhartia, Bradford Fisher, Peter Leonard, TOMS/N7 MS SO2 Vertical Column 1-Orbit L2 Swath 50x50 km V2.00, Greenbelt, MD, USA, Goddard Earth Sciences Data and Information Services Center (GES DISC), Accessed: May 10 2019, doi: 10.5067/MEASURES/SO2/DATA202, 2017

5   Krueger, A.J.: Sighting of El Chichón sulfur dioxide clouds with the Nimbus 7 total ozone mapping spectrometer, Science 220, 1377–1379, https://doi.org/10.1126/science.220.4604.1377, 1983.

Krueger, A. J., L. S. Walter, P. K. Bhartia, C. C. Schnetzler, N. A. Krotkov, I. Sprod, and G. J. S. Bluth: Volcanic sulfur dioxide measurements from the total mapping spectrometer instruments, *J. Geophys. Res.*, **100**, 14,057-14076, https://doi.org/10.1029/95JD01222, 1995.

10 Krueger, A. J., S. J. Schaefer, N. A. Krotkov, G. J. S. Bluth, and S. Barker: Ultraviolet remote sensing of volcanic emissions, in Remote Sensing of Active Volcanism, Geophys. Monogr. Ser., 116, edited by P. J. Mouginis-Mark, J. A. Crisp, and J. H. Fink, 25-43, http://doi.org/10.1029/GM116p0025, 2000.

Krueger, A.J., Krotkov, N.A., Carn, S.A.: El Chichon: the genesis of volcanic sulfur dioxide monitoring from space. J. Volcanol. Geotherm. Res. 175, 408-414. http://doi. org/10.1016/j.jvolgeores.2008.02.026,
15 2008.

Lee, C., Richter, A., Weber, M., Burrows, J.P.: SO₂ retrieval from SCIAMACHY using the weighting function DOAS (WFDOAS) technique: comparison with standard DOAS retrieval. Atmos. Chem. Phys. 8, 6137–6145. http://doi.org/10.5194/acp-8- 6137-2008, 2008.

Li, C., J. Joiner, N. A. Krotkov, P. K. Bhartia: A fast and sensitive new satellite retrieval algorithm
20 based on principal component analysis: application to the ozone monitoring instrument. *Geophys. Res. Lett.*, **40**, 6314 -6318, https://doi.org/10.1002/2013gl058134, 2013.

Li C., N. A. Krotkov, S. Carn, Y. Zhang, R. J. D. Spurr and J. Joiner: New generation NASA Aura Ozone Monitoring Instrument (OMI) volcanic SO2 dataset: algorithm description, initial results, and continuation with the Suomi-NPP Ozone Mapping and Profiler Suite (OMPS), *Atmos. Meas. Tech.*, **10**,
25 445-458, https://doi.org/10.5194/amt-10-445-2017, 2017.

Mankin, W. G. and M. T. Coffey: Increased stratospheric hydrogen chloride in the El Chichón cloud, *Science*, 226, 170-172, http://doi.org/10.1126/science.226.4671.170, 1984.

Mateer, C. L.., D. F. Heath, A. J. Krueger: Estimation of Total Ozone from Satellite Measurements of Backscattered Ultraviolet Earth Radiance, *J. Atmos. Sci.*, 28, 1307-1311, https://doi.org/10.1175/1520-
30 0469(1971)028<1307:EOTOFS>2.0.CO;2, 1971.

Molod, A., L. Takacs, M. Suarez, J. Bacmeister, I.-S. Song, and A. Eichmann: The GEOS-5 Atmospheric General Circulation Model: Mean Climate and Development from MERRA to Fortuna. *Technical Report Series on Global Modeling and Data Assimilation*, 28, 2012.

Ridley, D. A., S. Solomn, J. E. Barnes, V. D. Burlakov, T. Deshler, S. I. Dolgil, A. B. Herber, T. Nagai,
35 R. R. Neely III, A. V. Nevzorov, C. Ritter, T. Sakai, B. D. Santer, M. Sato, A. Schmidt, O. Uchino, J. P

Vernier: Total volcanic stratospheric aerosol optical depths and implications for global climate change, Geophys. Res. Lett., 41, 7763–7769, http://doi.org/10.1002/2014GL061541, 2014.

Robock, A.: Volcanic eruptions and climate: *Rev. of Geophys.*, 38, 191-219, https://doi.org/10.1029/1998RG000054, 2000.

5 Rogers, C. D.: Inverse Methods for Atmospheric Soundings: Theory and Practice, Series on Atmospheric, Oceanic and Planetary Physics, 2, World Scientific, 2000.

Rose, W.I., Gu, Y., Watson, I.M., Yu, T., Bluth, G.J.S., Prata, A.J., Krueger, A.J., Krotkov, N., Carn, S., Fromm, M.D., Hunton, D.E., Viggiano, A.A., Miller, T.M., Ballentin, J.O., Ernst, G.G.J., Reeves, J.M., Wilson, C. and Anderson, B.E. 2003. The February-March 2000 eruption of Hekla, Iceland from a 10 satellite perspective, in: Volcanism and the Earth's Atmosphere**,** edited by: Robock A. and Oppenheimer, C., AGU Geophysical Monograph 139, 107-132, 2003.

Solomon, S., R. W. Portmann, R. R. Garcia, W. Randel, F. Wu, R. Nagatani, J. Gleason, L., Thomason, L. R. Poole and M. P. McCormick: Ozone Depletion at mid-latitudes: coupling of volcanic aerosols and temperature variability to anthropogenic chlorine, *Geophys. Res. Lett*, 25, 1871-15 1874, https://doi.org/10.1029/98GL01293, 1998.

Solomon, S., Daniel, J.S., Neely III, R.R., Vernier, J.-P., Dutton, E.G., Thomason, L.W.: The persistently variable "background" stratospheric aerosol layer and global climate change, *Science*, 333, 866–870, http://doi.org/10.1126/science.1206027, 2011.

Spurr, R, and M. Christi, The LIDORT and VLIDORT Linearized Scalar and Vector Discrete Ordinate 20 Radiative Transfer Models: Updates in the last 10 Years. *Light Scattering Reviews*, Volume 12, ed. A. Kokhanovsky, Springer, 2019

Theys N., I. De Smedt, J. van Gent, T. Danckaert, T. Wang, F. Hendrick, T. Stavrakou, S. Bauduin, L. Clarisse, C. Li, N. Krotkov, H. Yu, H. Benot, M. Van Roozendael: Sulfur dioxide vertical column DOAS retrievals from the Ozone Monitoring Instrument: Global observations and comparison to 25 ground-based and satellite data. *J. Geophys. Res. Atmospheres*, 120, 2470-2491, http://doi.org/ 10.1002/2014JD022657, 2015.

Vernier, J.P., et al.: Major influence of tropical volcanic eruptions on the stratospheric aerosol layer during the last decade, *Geophys. Res. Lett.* 38, https://doi.org/10.1029/2011GL047563, 2011.